Discrete shedding of secondary vortices along Kaden's spiral

Diego Francescangeli, Karen Mulleners*

Institute of Mechanical Engineering, École polytechnique fédérale de Lausanne, Switzerland
* Corresponding author: karen.mulleners@epfl.ch

(Received xx; revised xx; accepted xx)

Abstract

When an object is accelerated in a fluid, a primary vortex is formed through the roll-up of a shear layer. This primary vortex does not grow indefinitely and will reach a limiting size and strength. Additional vorticity beyond the critical limit will end up in a trailing shear layer and accumulate into secondary vortices. The secondary vortices are typically considerably smaller than the primary vortex. In this paper, we focus on the formation, shedding, and trajectory of secondary vortices generated by a rotating rectangular plate in a quiescent fluid using time-resolved particle image velocimetry. The Reynolds number Rebased on the maximum rotational velocity of the plate is varied from 1680 to 22 300. At low Re, the shear layer is a continuous uninterrupted layer of vorticity that rolls up into a single coherent primary vortex. At $Re = 3910$, the shear layer becomes unstable and secondary vortices emerge away for the tip of the plate. For $Re > 3910$, secondary vortices are discretely released from the plate tip and are not generated from the stretching of an unstable shear layer. We demonstrate that the roll-up of the shear layer and the spatiotemporal location of secondary vortices can be described by a Kaden spiral for the entire Rerange considered. Based on the vorticity distribution along the time-varying Kaden spiral, we observed a constant convective time delay between successive secondary vortices of $\Delta\alpha = 20°$. This time-delay corresponds to a constant Strouhal number of 0.14 based on the plate's thickness.

1. Introduction

The life of vortices around bluff bodies often begins with a shear layer (Fernando *et al.* 2017; Jeon & Gharib 2004; Rosi & Rival 2017; Fernando & Rival 2016; Corkery *et al.* 2019). When a bluff body moves relative to a fluid flow, a thin layer of fluid emerges at the edge of the body where non-zero shear flow gradients are present. This shear layer is characterised by increased values of the flow vorticity. In the wake of the body, the shear layer rolls-up and the shear layer vorticity accumulates into a coherent vortex. The interplay between the free stream or body's velocity and the induced velocity of the growing coherent vortex cause the shear layer to become curved. This curvature changes continuously in time. The roll-up of a semi-infinite shear layer or vortex sheet was first described by Kaden (1931), who derived the following self-similar equation to describe the shear layer shape at any point in time t:

$$r = K(t/\theta)^{2/3} \tag{1.1}$$

where r and θ are the radial and tangential coordinates along the spiral with $r = 0$ at the spiral centre and K a dimensional constant. The exponent 2/3 is retrieved from

dimensional analysis and the obtained curve is a spiral with circular turns. The initial strength of the flat sheet increases monotonically with increasing distance away from the tip of the body. For $t > 0$, the spiral has an infinite number of turns leading to a singularity of the velocity and the sheet strength decreases to zero for $\theta \to \infty$ in the spiral centre. The maximum value of the sheet strength is now located somewhere along the sheet (Saffman 1995). In reality, viscosity will remove any singularity at the spiral centre and yield the development of a viscous core (Moore *et al.* 1973).

At the early stages of the roll-up, Kaden's spiral with circular turns is an accurate representation of the evolution of the shear layer. At later stages, the spiral turns become more elliptical than circular due to the viscous interactions within the shear layer and between the shear layer and the coherent primary vortex that grows due to the continuous accumulation of vorticity at the centre of the spiral. The distortions can be investigated by modelling the inner portion of the spiral as a single point vortex located at the centre (Moore 1974). The entire shear layer roll-up can also be predicted by a point-vortex representation of an initially straight vortex sheet (Krasny 1987; DeVoria & Mohseni 2018). The degree of the elliptical distortions depends on the shape of the object. They are almost negligible for flat plates and become more pronounced when the edge has a non-zero wedge angle (Pullin 1978).

The accumulation of the vorticity in the coherent vortex in the spiral centre does not continue indefinitely. There is a physical limit to the size and the amount of circulation the primary vortex can collect (Gharib *et al.* 1998; Mohseni & Gharib 1998; Gao & Yu 2010; de Guyon & Mulleners 2020). When the primary vortex is about to pinch-off, a trailing pressure maximum is observed along the shear layer (Lawson & Dawson 2013). The shear layer region between the tip and the trailing pressure maximum has an adverse pressure gradient. The remaining portion of the shear layer is characterised by a positive pressure gradient. The two regions of the shear layer are now separated and the vorticity associated with the adverse pressure gradient can not be entrained into the vortex core. The trailing pressure maximum travels downstream together with the primary vortex, causing the subsequent pinch-off of the primary vortex (Schlueter-Kuck & Dabiri 2016). Additional vorticity will not be entrained by the primary vortex after pinch-off and instead can accumulate into smaller secondary vortices within the trailing shear layer similar to a Kelvin-Helmholtz instability (Dabiri 2009). The increases in shear layer curvature during the initial stages of the vortex formation momentarily stops when the end of the primary vortex growth is reached (Sattari *et al.* 2012). Secondary vortices occur first between the primary vortex and the tip at locations where the sheet strength according to Kaden is maximal (Moore 1974; Koumoutsakos & Shiels 1996).

The emergence of secondary vortices seem to occur only if the Reynolds number is above a critical threshold. The value of this critical Reynolds number varies for different object geometries and boundary conditions. Critical values in a range from Re =1000 to 3000 were observed in a cylinder wake by Wu *et al.* (1996). The lower limit was slightly higher for Bloor (1964), who did not detect any instabilities for $Re < 1300$. The span-wise and end configurations strongly affect the shear layer breaking behind a cylinder. Parallel and oblique vortex shedding are obtained by changing the inclination of end plates (Prasad & Williamson 1997). The shear layer manifests instabilities at $Re = 1200$ for parallel shedding and at $Re = 2600$ for oblique shedding. The critical Reynolds number for an accelerated sharp edged plate lies in a higher range. Pullin & Perry (1980); Williamson (1996) started to visually observed secondary vortices along the shear layer for $Re = 4268$. This value was later confirmed by Luchini & Tognaccini (2002), who numerically observed the occurrence of secondary vortices in a range from $Re = 4500$ to 5000.

For Reynolds numbers above the critical value, series of secondary vortices appear in the

trailing shear layer with a seemingly constant distance between them. The typical shear layer frequency in the wakes of cylinders is much higher than the frequency of the von Karman vortex street. A consensus about the exact relationship between the frequency of the primary vortex shedding f_{K} and the secondary of shear layer vortices f_{SL} has not yet been found. Bloor (1964) observed that the ratio between the characteristic frequencies varies with Reynolds number according to $f_{\text{K}}/f_{\text{SL}} = Re^{1/2}$. However, there is no consensus about the exponent value of the proposed relationship. Prasad & Williamson (1997) indicated that an exponent value of 0.67 works for Re up to 10^5 and **?** found 0.87 in the range from $Re = 1200$ to 11 000. No clear relationships are established in the situation of an isolated primary vortex. Based on the flow visualisation around a submerged flat plate, Grift *et al.* (2019) determined the shedding frequency of secondary vortices to lie in the range from 13 Hz to 20 Hz, for different values of acceleration, velocity, and immersion depth. The secondary vortex shedding frequency behind a vertical flat plate increases with increasing acceleration of the flat plate according to Rosi & Rival (2017). It is crucial to define a scaling parameter, such as the Strouhal frequency for the cylinder case, that allows for a more universal relationship between the shedding frequency or formation time of primary and secondary vortices as a function of the Reynolds number. Here, we present an experimental study of secondary vortices generated by a rotating flat plate in a quiescent fluid. The plate is rotated with a constant rotational velocity which is varied across different experiments. First, we determine the critical Reynolds number above which secondary vortices are observed in the shear layer behind the tip of the rotating plate. Second, we describe the path of secondary vortices and approximate it using Kaden's spiral. Finally, we estimate the timing of the secondary vortex shedding process and analyse the effect of the Reynolds number on the timing.

2. Experimental methods

A rectangular flat glass plate, with chord length $c = 8$ cm, span $s = 16$ cm and thickness $t = 2$ mm, is rotated about 180° in a water tank around its span-wise axis. The glass plate is stiff enough to not bend due to the interaction with water and its transparency prevents shadow regions when conducing particle image velocimetry (PIV). The experiments are conducted in an octagonal tank with an outer diameter of 0.75 m filled with water (Figure 1a).

The rotation mechanism is fastened to an outer aluminium frame such that the mid span of the plate is in the centre of the tank to limit wall interference effects. The kinematic input is given by a servo motor (Maxon RE 35) connected to a stainless steel shaft and transferred to the flat plate through a 1 : 1 conical coupling. A 1 : 19 gearbox is mounted on the motor to ensure high torque, speed, and acceleration. The rotational angle, speed, and acceleration are controlled via a Galil DMC-40 motion controller, which allows for accurate control of arbitrary motion profiles. The rotation programme is a trapezoidal rotational velocity profile with a fixed rotational amplitude of 180° (Figure 1b).

To ensure a continuous acceleration profile, the corners of the velocity trapezoid are smoothed. The maximum rotational speed Ω_{max} is varied from 30 °/s to 400 °/s. This leads to a chord-based Reynolds number $Re = (\Omega_{\text{max}} c^2)/(2\nu)$ ranging from 1680 to 22 300. The rotational acceleration $\dot{\Omega}$ is fixed at 1000 °/s^2.

The PIV images are recorded in the cross-sectional plane at the model mid span. A high-power pulsed light-emitting diodes (LED Pulsed System, ILA 5150 GmbH) is used to create a light sheet in the measurement plane. The applicability of high-power LED for PIV has been demonstrated previously by Willert *et al.* (2010); Krishna *et al.* (2018). Time-resolved PIV images are recorded with a Photron FASTCAM SA-X2 high speed

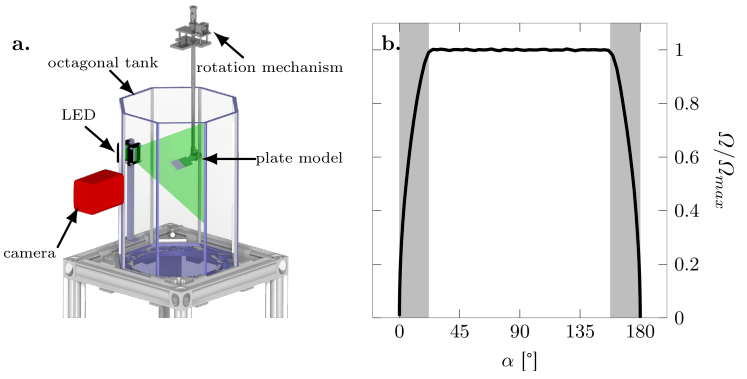

FIGURE 1. (a) Schematic of the experimental set-up and the rotation mechanism. (b) Trapezoidal velocity profile as a function of the angular position. The grey shaded regions indicate the portion of motion during which the plate is accelerated.

camera. The camera is equipped with a 35 mm Canon lens and the camera is aligned carefully such that the optical axis of the lens is aligned with the rotational axis of the plate and is perpendicular to the light sheet (Figure 1a). The frame rate and the exposure time are varied, depending on the dynamics of the motion. A frame rate and exposure time of 250 Hz and 1 ms are selected for a rotational speed of 30 °/s. These values are 2000 Hz and 0.5 ms for the highest tested speeds. The frame rate is high enough to capture the dynamics of the motion and the LED is set to continuous mode. The camera resolution is 1024 px × 1024 px, which corresponds to a field of view of 20 cm × 20 cm. The raw data are processed with a multi-pass algorithm with image deformation and a minimum squared difference correlation mode. The final interrogation window size is 16 px × 16 px with an overlap of 75 %. This yields a physical resolution of 1 mm or 0.02c.

3. Results

At $Re = 1680$, the plate rotation gives rise to the formation of a primary vortex (Figure 2). The velocity and vorticity fields at different angular positions are shown in the plate's frame of reference. The primary vortex is the only coherent structure that can be observed and it is connected to the plate tip through a continuous shear layer. No sign of instabilities are observed in the shear layer as the plate continues the rotation. The primary vortex moves along a path that matches the plate tip trajectory as indicated in Figure 2 by the dashed line. The shear layer remains connected to the primary vortex and rolls-up around its core. As a consequence, the shear layer evolves in time with a self-similar spiral shape. This observation is confirmed by Figure 3a, where the continuous shear layer is well described by Kaden's spiral (Equation 1.1). The spiral converges to its centre as $\theta \to \infty$ but for visual clarity, the spiral is only plotted for θ ranging from 0 to 4. The centre of the spiral is the centre of the primary vortex, computed as the maximum value of the Γ_2 function (Graftieaux *et al.* 2001). The top right edge of the plate is the point where the spiral ends.

Increasing the Reynolds number to 3910 results in the vorticity field shown in Figure 3b. The shear layer is now undulating and some localised concentrations of high vorticity can be identified along it. These are signs of an unstable shear layer. With a further increase of the Reynolds number to 16 760, the flow field topology changes again. The primary vortex is no longer connected to the plate tip and the shear layer is broken into a series of distinct individual structures that we refer to as secondary vortices (Figure 3c).

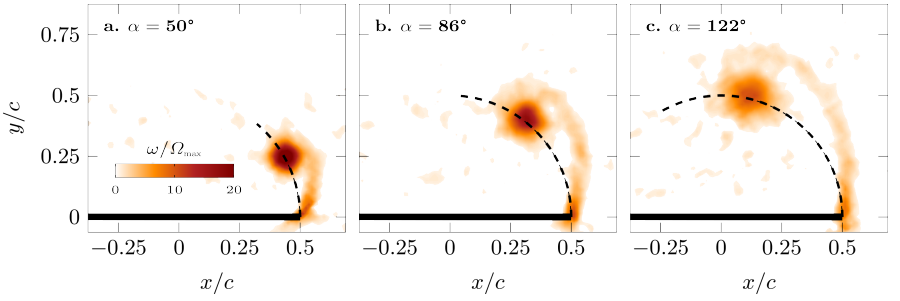

FIGURE 2. Vorticity fields of different angular positions (a) $\alpha = 50°$, (b) $\alpha = 86°$, and (c) $\alpha = 122°$ for $Re = 1680$. The dashed line represents the plate tip trajectory.

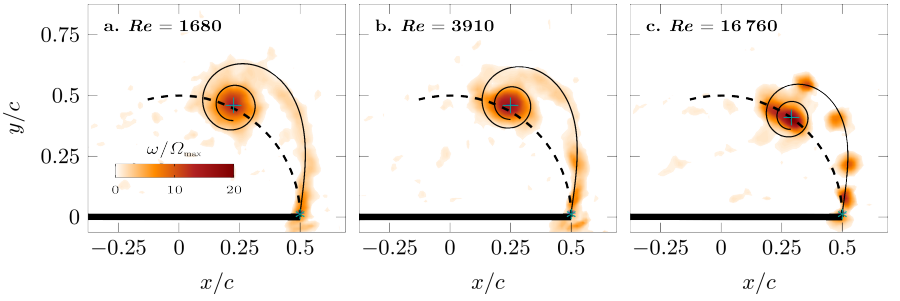

FIGURE 3. Kaden's spiral (black solid curve) atop of instantaneous vorticity fields at $\alpha = 105°$ for (a) $Re = 1680$, (b) $Re = 3910$, and (c) $Re = 16760$. The marker $*$ indicates the top right edge of the plate and the point where the spiral ends ($\theta = 0$), $+$ indicates the centre of the primary vortex and the point where the spiral begins ($\theta \to \infty$). The spiral is only plotted for θ ranging from 0 to 4. The dashed line represents the plate tip trajectory.

Kaden's equation still describes well the unstable shear layer evolution and the position of secondary vortices for the entire range of Reynolds number considered here.

The next step is to determine if these secondary vortices are generated from the stretching of an initially unstable shear layer or if they are discretely released after the separation of the primary vortex. Figure 4 shows the flow topology at different plate angular positions for $Re = 16\,760$.

Between 0° and 30° the primary vortex centre is close to the plate tip and no secondary vortices are observed. At 30°, the primary vortex has moved away from the tip along the circular tip trajectory and a first secondary vortex forms (Figure 4a). The first secondary vortex drifts towards the primary vortex core and they merge as a consequence of their mutual interaction(Figure 4b). The formation and shedding of successive secondary vortices is repeated along the entire motion. Each vortex is independently formed and subsequently released from the plate tip. In this situation, the shear layer appears as a cloud of vorticity close to the plate tip from which vortices are discretely detached. Even though they are not formed from the shear layer stretching, secondary vortices are still organised along a Kaden's spiral (Figure 4c-e). Only when the plate rotation is about to finish, vortices closer to the primary vortex slightly deviate from Kaden's curve (Figure 4f).

To characterise the formation process of secondary vortices, shed from a rotating plate, we use the time-varying Kaden spiral (Equation (1.1)). Once the secondary vortices shed, they move away and are located somewhere along the time-varying Kaden spiral (Figure 4). To estimate the timing of shedding of the individual vortices, we present the

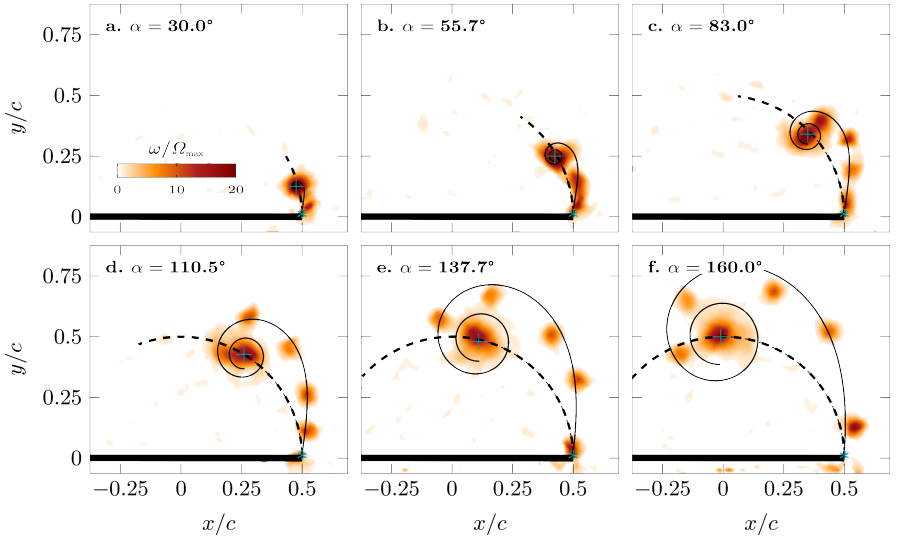

FIGURE 4. Temporal evolution of secondary vortices at different angular positions (a) $\alpha = 30.0°$, (b) $\alpha = 55.7°$, (c) $\alpha = 83.0°$, (d) $\alpha = 110.5°$, (e) $\alpha = 137.7°$, and (f) $\alpha = 160.0°$ for $Re = 16760$. The black curve is the Kaden's spiral, whose centre and end are the primary vortex centre (+) and the right top plate edge (∗). The spiral is only plotted for θ ranging from 0 to 4. The dashed line represents the plate tip trajectory.

spatiotemporal trajectory of the vortices along the shear layer in a space-time plot in Figure 5. We focus on the range between $\alpha = 30°$ and $\alpha = 170°$ when all secondary vortices form. At every time instant, we extract the vorticity along the Kaden spiral representing the roll-up at that time instant and combine this information in the form of a space-time diagram in Figure 5b. Only the spiral segment for θ ranging from 0 to 1.5π is considered which covers the locations of the secondary vortices. For $\theta > 1.5\pi$, secondary vortices start merging with the primary vortex. Figure 5a shows the spiral along which the vorticity is extracted for a selected snapshot at $\alpha = 100°$. The angular position of the plate is used as the dimensionless time variable. It corresponds to the ratio between the travelled arc length $l = \Omega tc/2$ and half of the chord length and thus represents a convective time scale. The length of the spiral varies in time and is normalised by the length of the spiral for $0 \leqslant \theta \leqslant 1.5\pi$ at $\alpha = 170°$. The spatial dimension along the normalised spiral length is indicated by L^*. Low values of L^* represent the spiral segment close to the plate tip, where vorticity is continuously produced and released. For the example rotation at $Re = 16\,760$ in Figure 5b, seven high vorticity bands can be identified and each of them represents an individually shed secondary vortex. The area of high vorticity for $L* < 0.2$ and $30° < \alpha < 40°$ represents the trace of the primary vortex. The first three secondary vortices will merge with the primary vortex before the end of the motion which explains why their traces do not continue until $\alpha = 170°$ in Figure 5b. The bands of high vorticity are separated by regions of zero vorticity, which corroborates the discrete release of secondary vortices during the rotation. The fourth and fifth bands are faded between $\alpha = 130°$ and $\alpha = 160°$. This is due to a slight deviation of the relative secondary vortices away from the Kaden spiral towards the primary vortex. This effect is attributed to a slight distortion of the outer and inner spiral turns when the rolling-up mechanism is about to finish, as discussed by Moore & Stuart (1975).

The space-time plots of the vorticity evolution along the shear layer are determined for $Re = 1680$ and $Re = 3910$ following the same procedure and the results are summarised

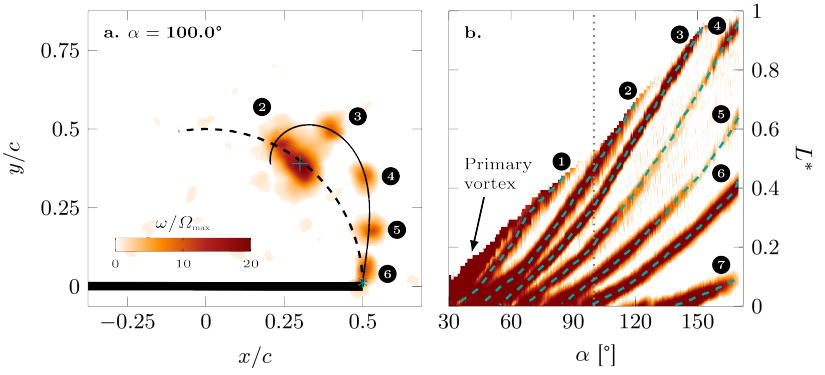

FIGURE 5. (a) Snapshot of the vorticity field at $\alpha = 100°$ with Kaden's spiral in black for $Re = 16\,760$. The spiral represents the path along which the vorticity is extracted. (b) Space-time representation of the vorticity along the spiral, for each plate angular position between $\alpha = 30°$ and $\alpha = 170°$. The bands of high vorticity concentration indicate the spatiotemporal evolution of secondary vortices along the spiral. The dashed lines mark the centrelines of these bands. The vertical dotted line marks the timing of the vorticity snapshot in (a).

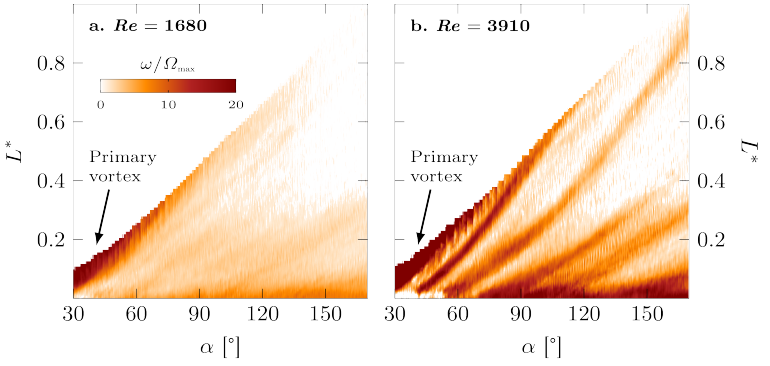

FIGURE 6. Space-time representations of the vorticity along the time-varying Kaden's spiral for (a) $Re = 1680$ and (b) $Re = 3910$.

in Figure 6. For the lowest Reynolds number $Re = 1680$, we have a continuous stable shear layer and the vorticity space-time plot shows a region of uniform vorticity, except for the primary vortex trace between $\alpha = 30°$ and $\alpha = 60°$ (Figure 6a). The lack of individually identifiable vorticity bands indicates that the shear layer is a continuous layer of fluid without the presence of any instabilities. For the intermediate Reynolds number $Re = 3910$, the shear layer is undulating and clear bands of high vorticity concentration can be identified in Figure 6b. These bands mark the position of instabilities along the spiral as highlighted in Figure 3b. In contrasts with Figure 5b, the bands are not separated by zero vorticity regions because of the presence of the unstable shear layer. Instabilities are formed along the shear layer away from the plate and are not discretely released at the tip of the plate. For all three regimes observed here, Kaden's spiral predicts the roll-up of the shear layer and the space-time evolution of the secondary vortices.

The timing of the shedding of secondary vortices can now be estimated based on the ridges in the vorticity space-time plots. The centreline of the high vorticity bands are indicated by the dashed lines in Figure 5b and their intersection with the horizontal axis corresponds to the timing of the secondary vortex shedding. To systematically extract the timing for various secondary vortices for rotational motions at different Reynolds

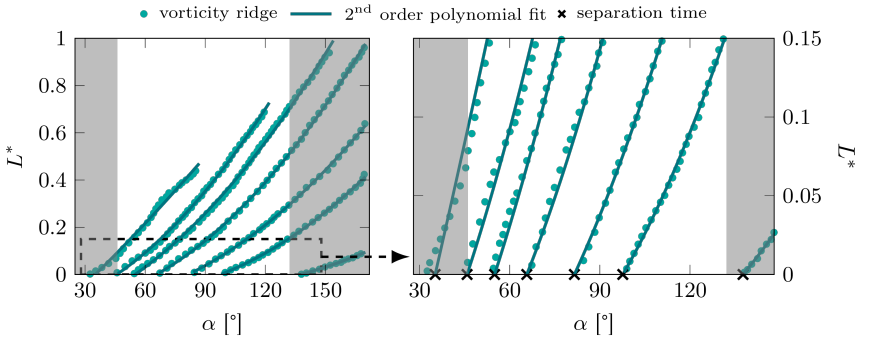

FIGURE 7. Second order polynomial fits of the ridge lines extracted from Figure 5. The grey shaded regions indicate the accelerating and decelerating parts of the motion while the black crosses represents instants at which vortices start moving downstream.

numbers, a second degree polynomial curve is used to fit the ridges (Figure 7). For the example case at $Re = 16\,760$ in Figure 7, seven ridges, corresponding to the seven secondary vortices, are identified. All fits have a R^2-value above 99 % which indicated the suitability of the second order polynomial approximation of the vorticity ridges. The positive root of the parabolic fit is now determined as the moment at which the vortex separates from the tip and starts moving along the spiral. The mean value of the differences between subsequent positive roots gives us the timing of the entire shedding process. For the example presented in Figure 7, the first secondary vortex is released after the plate has reached $\alpha = 35°$. The successive vortex shedding is repeated with an interval of $\Delta\alpha = 13° \pm 3°$, which corresponds to $\Delta t = 0.042$ s± 0.01 s (Figure 7). The timing delay changes prior to the shedding of the seventh secondary vortex, which does not shed until $\Delta\alpha = 40°$ after the pinch-off of the previous vortex. The plate starts decelerating around $\alpha = 132°$, while the last secondary vortex is still forming. The deceleration is assumed to delay the release of new secondary vortices.

The timing of the secondary vortex shedding as a function of Reynolds number is presented in Figure 8. Mean values and standard deviations are calculated based on 5 repetitions of the experiment at each Reynolds number. The dimensional time delay between the pinch-off of successive secondary vortices decreases and the shedding frequency thus increases with increasing Reynolds number (Figure 8a). In terms of convective time delay represented by the angular distance between subsequent vortices, we observe a constant delay of $\Delta\alpha = 20° \pm 8°$ for the entire range of Reynolds numbers considered here (Figure 8b). Even at $Re = 3910$, where the shear layer is unstable and secondary vortices are not discretely released, the shear layer instability creates secondary vortices with the same spacing.

The constant convective time delay between secondary vortices corresponds to a Strouhal number of 2.86 based on the semi-chord and a Strouhal number of 0.14 based on the plate's thickness. This suggests that the shear layer thickness and the scaling of the secondary vortex shedding is governed by the plate's thickness rather than its chord or length. It also suggests that all secondary vortices need the same convective time to form which is 10° to 15° less than the formation time of the primary vortex.

4. Conclusion

The roll-up of a shear layer behind a rotating plate in a quiescent fluid is experimentally studied for different rotational velocities or Reynolds numbers. Particular focus was

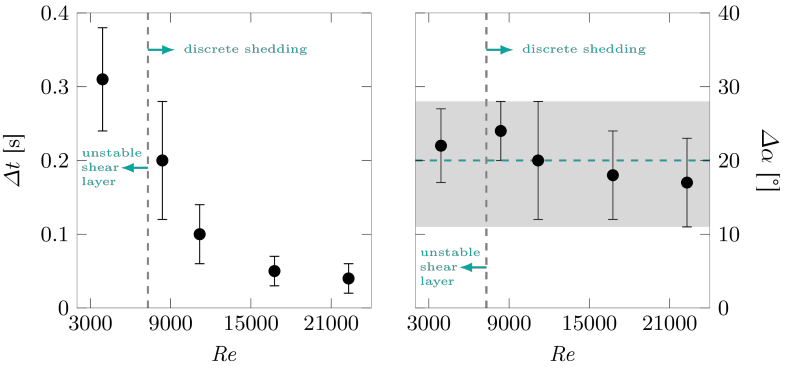

FIGURE 8. Delay between the successive shedding of secondary vortices in terms of (a) dimensional time and (b) convective time or angular distance between secondary vortices as a function of the Reynolds number. The grey area represents the range of values observed. The vertical dashed line separates the discrete shedding regime from the unstable shear layer case.

directed towards the formation, trajectory, and timing of secondary vortices. Time-resolved PIV at $Re = 1680$ revealed the roll-up of a continuous stable shear layer into a coherent primary vortex. At $Re = 3910$, the shear layer exhibits first signs of instabilities and secondary vortices appear as a result of a Kelvin-Helmholtz type instability of the shear layer away from the plate's tip. For $Re > 3910$, secondary vortices are discretely released from the plate's tip during the rotation and they do not form from the stretching of the shear layer. Both the shear layer and secondary vortices evolve in time along a self-similar spiral curve, which is well approximated by Kaden's equation. The Kaden spiral describes the spatiotemporal evolution of all secondary vortices. Based on the vorticity distribution along the time-varying Kaden spiral, the timing of the secondary vortex shedding is determined. The dimensional time delay between successive secondary vortices decreases with increasing Reynolds number. In terms of convective times this values is constant and secondary vortices are observed every $\Delta\alpha = 20°$ for all Reynolds numbers investigated. This corresponds to a constant Strouhal number of 0.14 based on the plate's thickness.

Declaration of interest

The authors report no conflict of interest.

REFERENCES

BLOOR, M. S. 1964 The transition to turbulence in the wake of a circular cylinder. *Journal of Fluid Mechanics* **19** (02), 290.

CORKERY, S. J., BABINSKY, H. & GRAHAM, W. R. 2019 Quantification of added-mass effects using particle image velocimetry data for a translating and rotating flat plate. *Journal of Fluid Mechanics* **870**, 492–518.

DABIRI, J. O. 2009 Optimal Vortex Formation as a Unifying Principle in Biological Propulsion. *Annual Review of Fluid Mechanics* **41** (1), 17–33.

DEVORIA, A. C. & MOHSENI, K. 2018 Vortex sheet roll-up revisited. *Journal of Fluid Mechanics* **855**, 299–321.

FERNANDO, J. N., MARZANEK, M., BOND, C. & RIVAL, D. E. 2017 On the separation mechanics of accelerating spheres. *Physics of Fluids* **29** (3), 037102.

FERNANDO, J. N. & RIVAL, D. E. 2016 On vortex evolution in the wake of axisymmetric and non-axisymmetric low-aspect-ratio accelerating plates. *Physics of Fluids* **28** (1), 017102.

Gao, L. & Yu, S. C. M. 2010 A model for the pinch-off process of the leading vortex ring in a starting jet. *Journal of Fluid Mechanics* **656**, 205–222.

Gharib, M., Rambod, E. & Shariff, K. 1998 A universal time scale for vortex ring formation. *Journal of Fluid Mechanics* **360**, 121–140.

Graftieaux, L., Michard, M. & Grosjean, N. 2001 Combining PIV, POD and vortex identification algorithms for the study of unsteady turbulent swirling flows. *Measurement Science and Technology* **12** (9), 1422–1429.

Grift, E. J., Vijayaragavan, N. B., Tummers, M. J. & Westerweel, J. 2019 Drag force on an accelerating submerged plate. *Journal of Fluid Mechanics* **866**, 369–398.

de Guyon, G. & Mulleners, K. 2020 Universal translational velocity of vortex rings behind conical objects, arXiv: 2009.05811.

Jeon, D. & Gharib, M. 2004 On the relationship between the vortex formation process and cylinder wake vortex patterns. *Journal of Fluid Mechanics* **519**, 161–181.

Kaden, H. 1931 Aufwicklung einer unstabilen Unstetigkeitsfläche. *Ing. Arch* **2** (2), 140–168.

Koumoutsakos, P. & Shiels, D. 1996 Simulations of the viscous flow normal to an impulsively started and uniformly accelerated flat plate. *Journal of Fluid Mechanics* **328**, 177–227.

Krasny, R. 1987 Computation of vortex sheet roll-up in the Trefftz plane. *J. Fluid Mech.* **184**, 123–155.

Krishna, S., Green, M. A. & Mulleners, K. 2018 Flowfield and Force Evolution for a Symmetric Hovering Flat-Plate Wing. *AIAA Journal* **56** (4), 1360–1371.

Lawson, J. M. & Dawson, J. R. 2013 The formation of turbulent vortex rings by synthetic jets. *Physics of Fluids* **25** (10), 105113.

Luchini, P. & Tognaccini, R. 2002 The start-up vortex issuing from a semi-infinite flat plate. *Journal of Fluid Mechanics* **455**, 175–193.

Mohseni, K. & Gharib, M. 1998 A model for universal time scale of vortex ring formation. *Physics of fluids* **10** (10), 2436.

Moore, D. W. 1974 A numerical study of the roll-up of a finite vortex sheet. *Journal of Fluid Mechanics* **63** (2), 225–235.

Moore, D. W., Saffman, P. G. & Stewartson, K. 1973 Axial flow in laminar trailing vortices. *Proceedings of the Royal Society of London. A. Mathematical and Physical Sciences* **333** (1595), 491–508.

Moore, D. W. & Stuart, J. T. 1975 The rolling up of a semi-infinite vortex sheet. *Proceedings of the Royal Society of London. A. Mathematical and Physical Sciences* **345** (1642), 417–430.

Prasad, A. & Williamson, C. H. K. 1997 The instability of the shear layer separating from a bluff body. *Journal of Fluid Mechanics* **333**, 375–402.

Pullin, D. I. 1978 The large-scale structure of unsteady self-similar rolled-up vortex sheets. *Journal of Fluid Mechanics* **88** (3), 401–430.

Pullin, D. I. & Perry, A. E. 1980 Some flow visualization experiments on the starting vortex. *Journal of Fluid Mechanics* **97** (2), 239–255.

Rosi, G. A. & Rival, D. E. 2017 Entrainment and topology of accelerating shear layers. *Journal of Fluid Mechanics* **811**, 37–50.

Saffman, P. G. 1995 *Vortex Dynamics*, 1st edn., *Cambridge Monographs on Mechanics and Applied Mathematics*, vol. 1. Cambridge ; New York: Cambridge University Press.

Sattari, P., Rival, D. E., Martinuzzi, R. J. & Tropea, C. 2012 Growth and separation of a start-up vortex from a two-dimensional shear layer. *Physics of Fluids* **24** (10), 107102.

Schlueter-Kuck, K. & Dabiri, J. O. 2016 Pressure evolution in the shear layer of forming vortex rings. *Physical Review Fluids* **1** (1), 012501.

Willert, C., Stasicki, B., Klinner, J. & Moessner, S. 2010 Pulsed operation of high-power light emitting diodes for imaging flow velocimetry. *Measurement Science and Technology* **21** (7), 075402.

Williamson, C. H. K. 1996 Vortex Dynamics in the Cylinder Wake. *Annual Review of Fluid Mechanics* **28** (1), 477–539.

Wu, J., Sheridan, J., Hourigan, K. & Soria, J. 1996 Shear layer vortices and longitudinal vortices in the near wake of a circular cylinder. *Experimental Thermal and Fluid Science* **12** (2), 169–174.